

Ferromagnetic Spin Glass State and Anomalous Hall Effect in Topological Semimetal Candidate $\text{Mn}_2\text{Sb}_2\text{Te}_5$

M.M. Sharma¹, Ankush Saxena², S.M. Huang², Santosh Karki Chhetri¹, Jin Hu^{1,3#}, V.P.S. Awana^{4*}

¹ *Department of Physics, University of Arkansas, Fayetteville, AR 72701, USA*

² *National Sun Yat-sen University, Kaohsiung, Taiwan - 804*

³ *Institute for Nanoscience and Engineering, MonArk NSF Quantum Foundry, and Smart Ferroic Materials Center, University of Arkansas, Fayetteville, Arkansas 72701, USA*

⁴ *CSIR- National Physical Laboratory, New Delhi 110012, India.*

Abstract:

Materials that intrinsically possess both magnetism and topological states represent a key frontier of quantum materials research. Recently, $\text{Mn}_2(\text{Bi}/\text{Sb})_2\text{Te}_5$ has emerged as a promising candidate for hosting topological surface states coupled with intrinsic magnetic order, making it a potential magnetic Weyl semimetal. In this study, we investigate the magnetic and transport properties of $\text{Mn}_2\text{Sb}_2\text{Te}_5$ single crystals. The magnetization measurements reveal a spin glass state with field-induced ferromagnetism. Although heat capacity measurement indicates the absence of long-range order, the intrinsic magnetization in $\text{Mn}_2\text{Sb}_2\text{Te}_5$ significantly affects its electrical properties, as demonstrated by the anomalous Hall effect. This work provides valuable insights into the magnetism and the electronic properties of $\text{Mn}_2\text{Sb}_2\text{Te}_5$, establishing $\text{Mn}_2(\text{Bi}/\text{Sb})_2\text{Te}_5$ system as a compelling platform for exploring the interplay between magnetism and non-trivial band topology, enabling emergent quantum phases and novel transport responses not accessible in non-magnetic systems.

Keywords – Spin glass state, AC susceptibility, magnetic topological materials, Anomalous Hall Effect.

#jinhu@uark.edu

*awana@nplindia.org

Introduction

Topological materials have attracted extensive attention recently due to their remarkable properties. A defining characteristic of these materials is the presence of conducting surface/edge topological states in topological insulators, while the nature of the bulk energy gap plays a critical role in shaping their exotic behaviours [1–4]. Magnetic topological insulators are a distinct class that exhibit a magnetically ordered bulk phase alongside the topological surface states [3,5,6]. The interplay between non-trivial band topology and bulk magnetic ordering in magnetic topological insulators leads to unique transport phenomena such as the quantum anomalous Hall effect [6–8], axion insulator state [9–11], and topological magneto-electric effect [12,13]. Beyond their fundamental interest, magnetic topological materials are also of considerable technological importance [3,5]. The coupling between magnetic order and topological electronic states enables control of Berry curvature and spin-polarized transport through external magnetic fields or magnetic engineering [3,6]. Such tunability can lead to dissipationless edge conduction, robust anomalous Hall responses, and magnetically switchable topological phases [6-8]. These properties make magnetic topological materials promising candidates for next-generation spintronic devices, topological memory elements, and low-power quantum electronic technologies [3,5]. Recent efforts have been focused on inducing bulk magnetic ordering in topological materials, including the fabrication of heterostructures consisting of magnetic and topological insulator layers [14–16] and doping topological insulators with magnetic atoms [17–19]. These methods, however, present challenges such as experimental complexity and defects. The challenges can be overcome by developing intrinsic materials with bulk magnetic ordering and non-trivial band topology. Topological insulators such as Bi_2Se_3 and Sb_2Te_3 feature layered structures separated by van der Waals gaps, allowing for the insertion of additional atomic layers to create natural

heterostructures, offering a versatile platform for tuning the quantum properties of topological insulators [20–23].

In this context, the $\text{Mn}(\text{Bi/Sb})_{2n}\text{Te}_{3n+1}$ ($n=1,2,3\dots$) family has been extensively studied. These materials are formed from MnTe layers embedded within multiple $(\text{Bi/Sb})_2\text{Te}_3$ unit cells [24–28]. The MnTe layers induce antiferromagnetic (AFM) or ferromagnetic (FM) ordering in the system, depending on the nature of the coupling of Mn spins [29–31]. The first member in this series, MnBi_2Te_4 , is an AFM magnetic topological insulator that hosts a magnetic field-driven Weyl state [26] and exhibit quantum anomalous Hall effect [8]. Theoretical studies also suggest that MnBi_2Te_4 can host a topological axion state [11,32]. The Sb-based compound, MnSb_2Te_4 , displays field-induced FM ordering with spin glass features [33,34] and can be tuned to a Weyl semimetal under pressure [35].

So far, most studies have focused on compounds with a single MnTe layer in $(\text{Bi/Sb})_2\text{Te}_3$ cells, i.e., MnBi_2Te_4 [8,32], while experimental studies on these with multiple MnTe layers remain less explored. Theoretical studies suggest that $\text{Mn}_2\text{Bi}_2\text{Te}_5$ with two MnTe layers in $(\text{Bi/Sb})_2\text{Te}_3$ cells could provide an ideal platform for realizing an axion insulator phase [36,37]. Recent study reports the successful synthesis of $\text{Mn}_2\text{Bi}_2\text{Te}_5$ single crystals with an ABC-type stacking of nine atomic layers (Te-Bi-Te-Mn-Te-Mn-Te-Bi-Te), where two Mn atoms have opposite spin orientations that give rise to an AFM ordering [38]. The Sb-based compound, $\text{Mn}_2\text{Sb}_2\text{Te}_5$, shows a FM order [39]. Theoretical studies predict $\text{Mn}_2(\text{Bi/Sb})_2\text{Te}_5$ can host topological surface states [40,41]. $\text{Mn}_2\text{Sb}_2\text{Te}_5$ is predicted to possess a NiAs-type crystal structure with an AFM ground state which generates gapped Dirac states [40]. With the polarization of magnetic moment by external magnetic field, a topological phase transition into a Weyl state is expected, which is characterized by Weyl point very close to the Fermi level (~ 7 meV) [40]. This is in sharp contrast with the Bi-based counterpart compound $\text{Mn}_2\text{Bi}_2\text{Te}_5$, which shows a gapped Dirac state in the FM state [40].

Another well-known key feature of Mn-Sb-Te compounds is the intermixing of Mn and Sb atomic sites. This site mixing causes Mn atoms to exist in multiple valence states, such as Mn^{2+} and Mn^{3+} [33,42]. The coexistence of magnetic atoms in different valence states leads to the emergence of complex magnetic phenomena, including multiple magnetic orders, spin glass behaviour, and other frustrated magnetic states [33,43]. Such atomic site mixing can also have a significant impact on the electronic structure, potentially inducing charge carrier localization, similar to the behaviour observed in the $\text{Fe}_{1+y}(\text{Te}_{1-x}\text{Se}_x)$ system [44,45]. However, the influence of site mixing on the magnetic and electrical transport properties of $\text{Mn}_2\text{Sb}_2\text{Te}_5$ remains unexplored to the best of our knowledge. Despite several exotic properties predicted in theoretical calculations, the experimental studies on $\text{Mn}_2\text{Sb}_2\text{Te}_5$ are very few. In this work, we systematically studied the magnetic properties and their correlation with electronic properties of $\text{Mn}_2\text{Sb}_2\text{Te}_5$. AC susceptibility confirmed a spin-glass state, with strong FM correlations. A strong anomalous Hall effect is observed without any topological feature, indicating the absence of ferromagnetism-induced Weyl semi-metallic state. This study provides crucial insights into the complex interplay between magnetism and electronic properties in $\text{Mn}_2\text{Sb}_2\text{Te}_5$, highlighting the spin-glass behaviour and strong FM correlations in shaping its transport properties. This study not only advances the understanding of intrinsic magnetic topological materials but also offers a foundation for exploring novel quantum phases in the Mn-Sb-Te system.

Experiment

Single crystals of $\text{Mn}_2\text{Sb}_2\text{Te}_5$ were grown using a self-flux method following Ref. [39]. Mn, Sb, and Te powders were combined in stoichiometric ratios and thoroughly mixed with an agate mortar and pestle. The homogeneous mixture was then pelletized into rectangular shapes, vacuum-sealed in a quartz ampoule, and heated to 1000 °C over 8 hours, maintained at this temperature for 48 hours, and then slowly cooled to 600 °C over 120 hours before quenching

in water. Magnetization measurements were carried out using a Magnetic Property Measurement System (MPMS3 SQUID, Quantum Design), which enables high-sensitivity magnetization measurements over a wide temperature (400 K – 1.8 K) and magnetic-field range (± 7 T). Hall resistivity and specific heat measurements were performed using a Physical Property Measurement System (PPMS, Quantum Design), allowing controlled measurements of transport and thermal properties under variable temperature (400 K – 1.8 K) and magnetic field conditions (± 9 T).

Results and Discussion

Structural characterization of the $\text{Mn}_2\text{Sb}_2\text{Te}_5$ single crystal was carried out using Rietveld refinement of the powder XRD pattern, as presented in Fig. 1. $\text{Mn}_2\text{Sb}_2\text{Te}_5$ crystallizes in a trigonal structure with $P-3m1$ space group symmetry, as shown in the inset of Fig. 1. The experimental PXRD pattern shows an excellent match with the calculated profile, yielding goodness-of-fit parameters $R_p = 1.56$ and $R_{wp} = 2.55$, both within the acceptable range. The refined lattice parameters are $a = b = 4.253(6)$ Å and $c = 17.865(4)$ Å. $\text{Mn}_2\text{Sb}_2\text{Te}_5$ was reported to have antisite disorder of Sb and Mn atoms via XPS measurement in our earlier report [39], so antisite disorder was taken into account while performing structural refinement. Mn atoms were allowed to partially occupy the Sb ($2d$) site, while Sb atoms were permitted to occupy the Mn ($2c$) site. The refinement confirms substantial antisite disorder at both sites, with approximately 22% Sb atoms occupying the Mn ($2c$) site and 15% Mn atoms occupying the Sb ($2d$) site. The detailed structural parameters are summarized in Table 1.

Figures 2(a) and (b) show the temperature dependence of the magnetization of $\text{Mn}_2\text{Sb}_2\text{Te}_5$ measured under DC magnetic fields along the in-plane ($H\parallel ab$) and the out-of-plane ($H\parallel c$) directions. The magnetic moment begins to increase below 30 K, indicating magnetic ordering of the system. The slightly higher magnetization for $H\parallel c$ suggests an easy axis along

the c -axis. A peak-like feature is observed around 18 K when $H\parallel c$, as indicated by the red arrow in Fig. 2b. In our earlier report on $\text{Mn}_2\text{Sb}_2\text{Te}_5$, this anomaly near ~ 18 K was tentatively interpreted as Neel temperature [39], which was primarily based on DC magnetization measurements and analogy with related Mn-(Bi/Sb)-Te compounds. However, the present measurements suggest that the magnetic behaviour is more complex. For both field orientations, magnetizations measured with field below 1000 Oe exhibit irreversibility between zero field-cooling (ZFC) and field-cooling (FC) data below 15 K, which should be attributed to a spin glass state as will be shown below [33,46,47]. At higher fields above 2500 Oe, the FC and ZFC magnetization converge, both exhibit strong increase up on cooling, indicating strong FM correlations, which is further supported by hysteresis loop in field-dependent magnetization shown below. The observed results are consistent with the theoretical results [38], which indicate a magnetic field-driven FM state in $\text{Mn}_2\text{Sb}_2\text{Te}_5$.

The isothermal magnetization (M - H) for $H\parallel ab$ and $H\parallel c$ are shown in Figs. 2(c) and (d). For $H\parallel ab$, magnetization is linear at low field and temperatures, followed by a saturation behaviour at higher field. For $H\parallel c$, a small hysteresis loop is observed (Fig. 2d, inset) up to 20 K, which, together with the magnetization above 0.6 T, implying strong FM correlations. Above 20 K, magnetization displays linear field dependence, implying a paramagnetic state. Such observation indicates the peak at 18 K in temperature dependent magnetization (red arrow in Fig. 1b) may correspond to magnetic phase transition. Additionally, below 10 K, isothermal magnetization shows a two-step behaviour at 0.5 kOe and 5 kOe, marked by arrows in the inset of Fig. 2(d), which suggests the presence of two magnetic states polarizing at different fields. A similar feature was observed in $\text{Mn}_2\text{Bi}_2\text{Te}_5$ at higher fields [38].

The formation of a spin glass state below 15 K can be demonstrated by the frequency-dependent freezing temperature (T_f) in AC susceptibility measurements [48–50]. AC susceptibility measurements were performed with magnetic field along the c -axis, using a zero

DC background and an AC field of 5 Oe with frequency f varying from 250 Hz to 10 kHz. Figure 3(a) depicts the variation of real (χ') and imaginary (χ'') parts of AC susceptibility with temperature. Two prominent peaks at $T_f \sim 11$ K and $T_c \sim 18$ K are observed, corresponding to the freezing temperature and magnetic ordering temperature. Minor features such as a weak shoulder around ~ 15 K and a broad feature near ~ 40 K are also visible in the AC susceptibility data. However, these features are not observed in DC magnetization. Therefore, they are unlikely to correspond to intrinsic magnetic phase transitions and are most likely related to background or instrumental effects inherent to AC susceptibility measurements. T_f in both χ' and χ'' shifts towards higher temperature as the frequency of the AC field is increased - a typical spin glass characteristic. Such a shift with frequency is clearly visible in the inset of Fig. 3(a), which shows the zoomed plot of $\chi'(T)$ near T_f . On the other hand, no shift in $T_c \sim 18$ K is observed, implying a possible static nature of the corresponding magnetic phase transition. Similar two peaks in AC susceptibility have been observed for $\text{Mn}_{1+x}\text{Sb}_{2-x}\text{Te}_4$, which were designated to two different spin glass states [42], but in the present case, it is hard to relate both susceptibility peaks to spin glass due to the lack of frequency dependence at T_c . In fact, the frequency-independent AC susceptibility peak at T_c followed by the frequency-dependent peak at T_f is reminiscent of reentrant spin-glass systems [51], where the ferromagnetic ordering established below T_c becomes unstable at lower temperatures as randomness and competing exchange interactions dominate. Consequently, the spins gradually lose coherence and freeze into a disordered, non-equilibrium configuration below T_f . This transition reflects a crossover from an ordered ferromagnetic to a frozen spin-glass-like state [51]. The observed behaviour is consistent with that reported for well-established systems exhibiting a reentrant spin-glass state, such as magnetic alloys [47,52] and manganites [53]. The observed spin glass feature may stem from the presence of Mn^{2+} and Mn^{3+} mixed ions, as revealed by X-ray photoelectron spectroscopy measurements [39]. Cation mixing, common in the Mn-Sb-Te family [33,42],

results in antisite defects where some Mn atoms occupy Sb^{3+} sites, which gives rise to Mn^{3+} . The presence of antisite defects in $\text{Mn}_2\text{Sb}_2\text{Te}_5$ is evidenced from the Rietveld refined XRD pattern, which shows that both Mn and Sb atoms are interchanging their atomic positions. Cationic mixing may also induce atomic short-range order, influencing local magnetic interactions. The coexistence of multiple valence states in magnetic ions often leads to spin glass states due to competing magnetic interactions as observed in MnSb_2Te_4 [33], manganites [54] and double perovskite [55].

For spin glass, the relative shift in freezing temperature per frequency decade is calculated as $\delta T_f = \frac{\Delta T_f}{T_f \Delta(\log_{10} \nu)}$ where $\nu = 2\pi f$ is the angular frequency. The obtained δT_f of 0.02 lies within the range of $0.0045 \leq \delta T_f \leq 0.08$ for canonical spin glass systems [56]. Further analysis of the spin glass behaviour was conducted by examining the frequency dependence of the freezing temperature T_f . Conventionally, this dependence follows a power law [46,56]:

$$\tau = \tau_0 \left(\frac{T_f - T_{SG}}{T_{SG}} \right)^{-n} \quad (1)$$

where τ is the relaxation time corresponding to the AC frequency ($\tau = 1/2\pi f = 1/\nu$), τ_0 is the characteristic relaxation time of a single spin flip, T_{SG} is the zero-frequency spin-glass temperature, and the term $\left(\frac{T_f - T_{SG}}{T_{SG}} \right)$ represents reduced temperature t . Here $T_{SG} \sim 10.62\text{K}$ can be extracted by extrapolating the frequency dependence for T_f . Figure 3(b) depicts the experimentally determined relaxation time τ as a function of the reduced temperature t , the fitting of which with the above Eq. 1 yields $\tau_0 = 5.01(6) \times 10^{-8}$ s. This value is much higher than 10^{-12} s, the typical value for a canonical spin glass system [49], suggesting the presence of strongly interacting clusters in $\text{Mn}_2\text{Sb}_2\text{Te}_5$. The presence of clusters can be verified by the deviation from the Arrhenius formalism $\nu = \nu_0 \exp\left(\frac{-E_a}{k_B T_f}\right)$, where E_a denotes the activation energy, and k_B is the Boltzmann constant. This is because that the spin dynamics controlled by

single spin flips tends to follow the Arrhenius law [46,56]. However, as shown in Fig. 3(c), the linear dependence between $\ln(\nu)$ and $1/T_f$ expected from the above Arrhenius formalism does not hold for $\text{Mn}_2\text{Sb}_2\text{Te}_5$, especially at the low frequency regime. This deviation implies collective spin freezing in $\text{Mn}_2\text{Sb}_2\text{Te}_5$, which is better modelled by the empirical Vogel-Fulcher law [46,57]:

$$\nu = \nu_0 \exp\left(\frac{-E_a}{k_B(T_f - T_0)}\right) \quad (2)$$

where T_0 is the Vogel-Fulcher temperature, and ν_0 is the characteristic frequency that can be extracted from the characteristic relaxation time τ_0 obtained above through $\nu_0 = 1/\tau_0$. As shown in Fig. 3(d), Vogel-Fulcher law reproduces the data very well, yielding an activation energy E_a of 0.97 meV and Vogel-Fulcher temperature T_0 of 9.65 K. The non-zero value of T_0 indicates the presence of interactions among spins of different magnetic ions, forming a cluster spin glass [49,50,58].

To gain more insight into magnetism in $\text{Mn}_2\text{Sb}_2\text{Te}_5$, heat capacity measurements have been performed to detect bulk magnetic ordering. As shown in Fig. 4, no clear anomaly has been observed in heat capacity near 18 K, where ferromagnetic ordering appears according to magnetic measurements. However, a small deviation between the zero-field and 9 T heat capacity emerges around this temperature (lower inset of Fig. 4) that could be attributed to the onset of ferromagnetic correlations. The absence of a sharp λ -type anomaly suggests that the magnetic transition is broad and involves a gradual development of magnetic order rather than a well-defined long-range transition. Such behaviour is characteristic of reentrant cluster spin-glass systems [53,59], where the total magnetic contribution to the specific heat is small and indicates a small change in entropy at the transition.

Ignoring magnetic contributions, the low-temperature heat capacity C can be expressed as

$$C = \gamma T + \beta T^3 \quad (3)$$

where γ is the Sommerfeld coefficient and related to the electronic contribution γT to heat capacity, and βT^3 is the phonon contribution. Providing that the magnetic contribution is rather weak as demonstrated by the negligible impact of magnetic field on the heat capacity, the above Eq. 3 was used to analysis the measured heat capacity. As shown in the upper inset of Fig. 3, the fit of C/T to $\gamma + \beta T^2$ yield $\gamma = 0.14(1) \text{ Jmol}^{-1}\text{K}^{-2}$ and $\beta = 0.0036(3) \text{ Jmol}^{-1}\text{K}^{-2}$. From the obtained β , Debye temperature θ_D for $\text{Mn}_2\text{Sb}_2\text{Te}_5$ was calculated as $116 \pm 1 \text{ K}$ via $\theta_D = \left(\frac{12\pi^4 nR}{5\beta_n}\right)^{1/3}$ where R is the ideal gas constant. The obtained value of γ is quite high as compared to normal metals. Such enhanced γ value is comparable to that of reported spin glass systems [49,60–62], which can be understood in terms of competing magnetic interactions that gives rise to a high degree of frustrations [56].

$\text{Mn}_2\text{Sb}_2\text{Te}_5$ exhibits various magnetic phases, which have been summarized in the field (H)-temperature (T) phase diagram shown in Fig. 5. This phase diagram shows the evolution from the paramagnetic state into a regime of short-range ferromagnetic correlations below $T_c \approx 18 \text{ K}$, followed by reentrant freezing into a ferromagnetic cluster spin-glass state below $T_f \approx 11 \text{ K}$ at low fields. It also illustrates the suppression of glassy freezing and the emergence of a field-polarized FM-like state under an applied magnetic field of 2.5 kOe. The observed magnetic properties in $\text{Mn}_2\text{Sb}_2\text{Te}_5$ are in sharp contrast with its Bi analogue, which shows a clear AFM transition. This might be attributed to the nature of the present antisite defect. Mn-Sb antisite disorder is expected to be more pronounced than Mn-Bi antisite disorder [63], which enhances Mn/Sb site mixing and mixed $\text{Mn}^{2+}/\text{Mn}^{3+}$ valence, introduces competing magnetic

exchange interactions, which frustrate long-range magnetic order and stabilizes a glassy magnetic ground state in $\text{Mn}_2\text{Sb}_2\text{Te}_5$.

With the understanding of magnetism in $\text{Mn}_2\text{Sb}_2\text{Te}_5$, its impact on transport is studied via the anomalous Hall effect. The magnetic field ($\mu_0 H$) dependent transverse (Hall) resistivity (ρ_{yx}) is shown in Fig. 6(a). The positive slope indicates p -type charge carriers in $\text{Mn}_2\text{Sb}_2\text{Te}_5$, which is in sharp contrast to $\text{Mn}_2\text{Bi}_2\text{Te}_5$, that possess electron-type carriers [38]. A similar change in carrier type has also been observed in MnBi_2Te_4 [8] and MnSb_2Te_4 [64]. Carrier concentration, based on the Hall resistivity slope, is approximately $3.67 \times 10^{20} \text{ cm}^{-3}$ at 2 K. Near zero field, the non-zero Hall resistivity and Hall resistivity loop (Fig. 6b) reflect an anomalous Hall effect (*AHE*). The close resemblance between Hall resistivity loop (Fig. 6b) and the magnetization loop (Fig. 3b), as well as their similar temperature dependence, indicates a magnetic origin for *AHE*. To further elaborate on the coupling between magnetic and electrical properties in the studied $\text{Mn}_2\text{Sb}_2\text{Te}_5$, the derivative of Hall resistivity and magnetization with respect to $\mu_0 H$ has been plotted together in the inset of Fig. 6(a). The field-induced steps in Hall resistivity align with magnetization measurements, as shown by arrows in the inset of Fig. 6(a). Similar coupled transport and magnetization properties were also observed in its sister compound, $\text{Mn}_2\text{Bi}_2\text{Te}_5$ [38]. Interestingly, despite the absence of long-range magnetic order, $\text{Mn}_2\text{Sb}_2\text{Te}_5$ exhibits a strong anomalous Hall effect, which confirms the presence of robust FM correlations revealed in magnetization measurements. The observed *AHE* demonstrate that robust anomalous Hall responses can emerge from glassy and cluster-based magnetic states, and highlights that magnetic disorder and short-range correlations can strongly influence electronic transport in magnetic topological material candidates. Theoretically, the FM $\text{Mn}_2\text{Sb}_2\text{Te}_5$ is predicted to host a Weyl phase [40], which is reminiscent of the FM Weyl state up on the polarization of magnetic moment under magnetic field in $\text{Mn}(\text{Bi,Sb})_2\text{Te}_4$ [26,65,66]. In $\text{Mn}(\text{Bi,Sb})_2\text{Te}_4$, the transition to a FM Weyl state is manifested in a strong intrinsic

topological Hall effect [26]. However, the signature of topological Hall effect is not observed in $\text{Mn}_2\text{Sb}_2\text{Te}_5$. This might be due to the fact that the Weyl points are not close to the Fermi level, which is supported by rather high hole carrier density of 10^{20} cm^{-3} . Such a large carrier density implies that the chemical potential is pushed far away from the low-energy band features. As an order-of-magnitude estimate, treating the holes as a three-dimensional degenerate Fermi gas, Fermi energy can be calculated using the relation $E_F = \frac{\hbar^2 k_F^2}{2m^*}$, where k_F is Fermi wavevector and can be calculated by the hole density using the relation $p = \frac{k_F^3}{3\pi^2}$, for this analysis bare electron mass has been considered. For $p = 3.67 \times 10^{20} \text{ cm}^{-3}$, E_F is found to be $\sim 0.17 \text{ eV}$, much larger than the $\sim 0.7 \text{ meV}$ associated with Weyl nodes predicted in the ideal ferromagnetic state [40]. Consequently, any Weyl-related Berry-curvature contributions to transport are expected to be strongly masked by the large background of conventional carriers, and the Hall response is therefore dominated by the ordinary and anomalous Hall components, consistent with the experimental observations.

This is in agreement with $\text{Mn}(\text{Bi,Sb})_2\text{Te}_4$, where clear Weyl-related transport signatures have been reported only when the carrier density is reduced to $\sim 10^{18} \text{ cm}^{-3}$ through careful Bi/Sb composition tuning [26]. Sb-rich compositions, which retain similarly high hole densities, do not show clear evidence of Weyl transport features. Motivated by this established trend, partial substitution of Sb by Bi in $\text{Mn}_2(\text{Bi/Sb})_2\text{Te}_5$ provides a plausible route to lower the carrier density and shift the chemical potential closer to the Weyl nodes, thereby improving the prospects for realising a magnetic Weyl semimetal state in this material family.

Conclusion:

In summary, we have demonstrated the magnetic, thermal, and electronic properties of $\text{Mn}_2\text{Sb}_2\text{Te}_5$, a potential new member to the family of magnetic topological materials. Unlike its Bi counterpart, $\text{Mn}_2\text{Bi}_2\text{Te}_5$ which exhibits AFM ordering, $\text{Mn}_2\text{Sb}_2\text{Te}_5$ displays a more complex

magnetism characterized by a spin glass state with strong FM correlations that is distinct from the predicted ground state. This complexity might be attributed to atomic site intermixing between Mn and Sb atoms. Additionally, the transverse magneto-transport measurement reveals AHE, highlighting the coupling between magnetic and electronic properties. However, the Weyl phase, which is anticipated in the FM phase of $\text{Mn}_2\text{Sb}_2\text{Te}_5$, remains elusive, which is likely because the Weyl point is too far from the Fermi energy as revealed by high carrier density. This study emphasizes the crucial role of atomic disorders in shaping the properties of $\text{Mn}_2\text{Sb}_2\text{Te}_5$. Further investigations, such as Bi substitution to lower the carrier density, could help in tuning its electronic and magnetic properties, potentially revealing the anticipated topological states and deepening the understanding of its topological nature.

Acknowledgement:

M.M. Sharma acknowledges support by μ -ATOMS, an Energy Frontier Research Center funded by DOE, Office of Science, Basic Energy Sciences, under Award DE-SC0023412. The use of MPMS3 SQUID is supported by MonArk NSF Quantum Foundry, which is supported by the National Science Foundation Q-AMASE-i program under NSF award No. DMR-1906383. Ankush Saxena acknowledges the financial support by the Ministry of Science and Technology R.O.C. Taiwan for Grant No. MOST-113-2112-M-110-018.

Data Availability Statement:

The data will be made available from the corresponding author upon reasonable request.

Table: Structural parameters of $\text{Mn}_2\text{Sb}_2\text{Te}_5$ obtained from Rietveld refinement of PXRD pattern.

Compound	Lattice parameters (Å)			Atoms	Wycoff	Atomic positions			Occ.
	<i>a</i>	<i>b</i>	<i>c</i>			<i>x</i>	<i>y</i>	<i>z</i>	
$\text{Mn}_2\text{Sb}_2\text{Te}_5$	4.253(7)	4.253(7)	17.870(0)	Mn1	<i>2c</i>	0.0000	0.0000	0.3463	0.775
				Sb1	<i>2c</i>	0.0000	0.0000	0.3463	0.220
				Mn2	<i>2d</i>	0.3333	0.6666	0.0823	0.150
				Sb2	<i>2d</i>	0.3333	0.6666	0.0823	0.854
				Te1	<i>1a</i>	0.0000	0.0000	0.0000	1.000
				Te2	<i>2d</i>	0.3333	0.6666	0.2049	1.000
				Te3	<i>2d</i>	0.3333	0.6666	0.4274	1.000

References:

- [1] M. Z. Hasan and C. L. Kane, Colloquium: Topological insulators, *Rev. Mod. Phys.* **82**, 3045 (2010).
- [2] X.-L. Qi and S.-C. Zhang, Topological insulators and superconductors, *Rev. Mod. Phys.* **83**, 1057 (2011).
- [3] Y. Tokura, K. Yasuda, and A. Tsukazaki, Magnetic topological insulators, *Nat Rev Phys* **1**, 126 (2019).
- [4] M. M. Sharma, P. Sharma, N. K. Karn, and V. P. S. Awana, Comprehensive review on topological superconducting materials and interfaces, *Supercond. Sci. Technol.* **35**, 083003 (2022).
- [5] B. A. Bernevig, C. Felser, and H. Beidenkopf, Progress and prospects in magnetic topological materials, *Nature* **603**, 41 (2022).
- [6] X. Kou, Y. Fan, M. Lang, P. Upadhyaya, and K. L. Wang, Magnetic topological insulators and quantum anomalous hall effect, *Solid State Communications* **215–216**, 34 (2015).
- [7] R. Gao, G. Qin, S. Qi, Z. Qiao, and W. Ren, Quantum anomalous Hall effect in MnBi_2Te_4 van der Waals heterostructures, *Phys. Rev. Materials* **5**, 114201 (2021).
- [8] Y. Deng, Y. Yu, M. Z. Shi, Z. Guo, Z. Xu, J. Wang, X. H. Chen, and Y. Zhang, Quantum anomalous Hall effect in intrinsic magnetic topological insulator MnBi_2Te_4 , *Science* **367**, 895 (2020).

- [9] R. Li, J. Wang, X.-L. Qi, and S.-C. Zhang, Dynamical axion field in topological magnetic insulators, *Nature Phys* **6**, 284 (2010).
- [10] C. Yue, Y. Xu, Z. Song, H. Weng, Y.-M. Lu, C. Fang, and X. Dai, Symmetry-enforced chiral hinge states and surface quantum anomalous Hall effect in the magnetic axion insulator $\text{Bi}_{2-x}\text{Sm}_x\text{Se}_3$, *Nat. Phys.* **15**, 577 (2019).
- [11] C. Liu, Y. Wang, H. Li, Y. Wu, Y. Li, J. Li, K. He, Y. Xu, J. Zhang, and Y. Wang, Robust axion insulator and Chern insulator phases in a two-dimensional antiferromagnetic topological insulator, *Nat. Mater.* **19**, 522 (2020).
- [12] Y. Wan, J. Li, and Q. Liu, Topological magnetoelectric response in ferromagnetic axion insulators, *National Science Review* **11**, nwac138 (2024).
- [13] Z. Liu and J. Wang, Anisotropic topological magnetoelectric effect in axion insulators, *Phys. Rev. B* **101**, 205130 (2020).
- [14] C.-Z. Chang et al., Thin Films of Magnetically Doped Topological Insulator with Carrier-Independent Long-Range Ferromagnetic Order, *Advanced Materials* **25**, 1065 (2013).
- [15] D. Zhang et al., Interplay between ferromagnetism, surface states, and quantum corrections in a magnetically doped topological insulator, *Phys. Rev. B* **86**, 205127 (2012).
- [16] Y. Fan et al., Magnetization switching through giant spin-orbit torque in a magnetically doped topological insulator heterostructure, *Nature Mater* **13**, 699 (2014).
- [17] J. G. Checkelsky, J. Ye, Y. Onose, Y. Iwasa, and Y. Tokura, Dirac-fermion-mediated ferromagnetism in a topological insulator, *Nature Phys* **8**, 729 (2012).
- [18] Y. Ou et al., Enhancing the Quantum Anomalous Hall Effect by Magnetic Codoping in a Topological Insulator, *Advanced Materials* **30**, 1703062 (2018).
- [19] X. Kou et al., Scale-Invariant Quantum Anomalous Hall Effect in Magnetic Topological Insulators beyond the Two-Dimensional Limit, *Phys. Rev. Lett.* **113**, 137201 (2014).
- [20] A. Saxena, N. K. Karn, M. M. Sharma, and V. P. S. Awana, Detailed structural and topological analysis of SnBi_2Te_4 single crystal, *Journal of Physics and Chemistry of Solids* **174**, 111169 (2023).
- [21] A. Saxena, M. M. Sharma, P. Sharma, Y. Kumar, P. Rani, M. Singh, S. Patnaik, and V. P. S. Awana, Structural and weak antilocalization analysis of topological single-crystal SnSb_2Te_4 , *Journal of Alloys and Compounds* **895**, 162553 (2022).
- [22] A. Marcinkova, J. K. Wang, C. Slavonic, A. H. Nevidomskyy, K. F. Kelly, Y. Filinchuk, and E. Morosan, Topological metal behavior in GeBi_2Te_4 single crystals, *Phys. Rev. B* **88**, 165128 (2013).
- [23] M. Nurmamat et al., Topologically Nontrivial Phase-Change Compound GeSb_2Te_4 , *ACS Nano* **14**, 9059 (2020).

- [24] C. Hu, T. Qian, and N. Ni, Recent progress in $\text{MnBi}_{2n}\text{Te}_{3n+1}$ intrinsic magnetic topological insulators: crystal growth, magnetism and chemical disorder, *Natl Sci Rev* **11**, nwad282 (2023).
- [25] R. Lu et al., Half-Magnetic Topological Insulator with Magnetization-Induced Dirac Gap at a Selected Surface, *Phys. Rev. X* **11**, 011039 (2021).
- [26] S. H. Lee et al., Evidence for a Magnetic-Field-Induced Ideal Type-II Weyl State in Antiferromagnetic Topological Insulator $\text{Mn}(\text{Bi}_{1-x}\text{Sb}_x)_2\text{Te}_4$, *Phys. Rev. X* **11**, 031032 (2021).
- [27] M. Sahoo et al., Ubiquitous Order-Disorder Transition in the Mn Antisite Sublattice of the $(\text{MnBi}_2\text{Te}_4)(\text{Bi}_2\text{Te}_3)$ Magnetic Topological Insulators, *Advanced Science* **n/a**, 2402753 (n.d.).
- [28] I. R. Amiraslanov, Z. S. Aliev, P. A. Askerova, E. H. Alizade, Y. N. Aliyeva, N. A. Abdullayev, Z. A. Jahangirli, M. M. Otrokov, N. T. Mamedov, and E. V. Chulkov, Crystal structure and Raman-active lattice vibrations of magnetic topological insulators $\text{MnBi}_2\text{Te}_4 \cdot n(\text{Bi}_2\text{Te}_3)$ ($n = 0, 1, \dots, 6$), *Phys. Rev. B* **106**, 184108 (2022).
- [29] X. Xu et al., Ferromagnetic-antiferromagnetic coexisting ground state and exchange bias effects in MnBi_4Te_7 and $\text{MnBi}_6\text{Te}_{10}$, *Nat Commun* **13**, 7646 (2022)
- [30] B. Chen et al., Even–Odd Layer-Dependent Exchange Bias Effect in MnBi_2Te_4 Chern Insulator Devices, *Nano Lett.* **24**, 8320 (2024).
- [31] A. Saxena, S.-M. Huang, N. K. Karn, M. M. Sharma, Kamal, C.-M. Lin, M. Chou, and V. P. S. Awana, Intrinsic coexistence of ferromagnetic and antiferromagnetic phases in MnSb_2Te_4 topological layers, *Journal of Magnetism and Magnetic Materials* **637**, 173696 (2026).
- [32] D. Zhang, M. Shi, T. Zhu, D. Xing, H. Zhang, and J. Wang, Topological Axion States in the Magnetic Insulator MnBi_2Te_4 with the Quantized Magnetoelectric Effect, *Phys. Rev. Lett.* **122**, 206401 (2019).
- [33] H. Li, Y. Li, Y. Lian, W. Xie, L. Chen, J. Zhang, Y. Wu, and S. Fan, Glassy magnetic ground state in layered compound MnSb_2Te_4 , *Sci. China Mater.* **65**, 477 (2022).
- [34] W. Ge, P. M. Sass, J. Yan, S. H. Lee, Z. Mao, and W. Wu, Direct evidence of ferromagnetism in MnSb_2Te_4 , *Phys. Rev. B* **103**, 134403 (2021).
- [35] H. Zhang, W. Yang, Y. Wang, and X. Xu, Tunable topological states in layered magnetic materials of MnSb_2Te_4 , MnBi_2Se_4 , and MnSb_2Se_4 , *Phys. Rev. B* **103**, 094433 (2021).
- [36] J. Zhang, D. Wang, M. Shi, T. Zhu, H. Zhang, and J. Wang, Large Dynamical Axion Field in Topological Antiferromagnetic Insulator $\text{Mn}_2\text{Bi}_2\text{Te}_5$, *Chinese Phys. Lett.* **37**, 077304 (2020).
- [37] Y. Li, Y. Jiang, J. Zhang, Z. Liu, Z. Yang, and J. Wang, Intrinsic topological phases in $\text{Mn}_2\text{Bi}_2\text{Te}_5$ tuned by the layer magnetization, *Phys. Rev. B* **102**, 121107 (2020).

- [38] L. Cao et al., Growth and characterization of the dynamical axion insulator candidate $\text{Mn}_2\text{Bi}_2\text{Te}_5$ with intrinsic antiferromagnetism, *Phys. Rev. B* **104**, 054421 (2021).
- [39] A. Saxena and V. P. S. Awana, Growth and characterization of the magnetic topological insulator candidate $\text{Mn}_2\text{Sb}_2\text{Te}_5$, *J. Phys.: Condens. Matter* **36**, 085704 (2023).
- [40] S. V. Ereemeev, M. M. Otrokov, A. Ernst, and E. V. Chulkov, Magnetic ordering and topology in $\text{Mn}_2\text{Bi}_2\text{Te}_5$ and $\text{Mn}_2\text{Sb}_2\text{Te}_5$ van der Waals materials, *Phys. Rev. B* **105**, 195105 (2022).
- [41] W. Yang, Y. Zhang, F. Wang, J. Peng, H. Zhang, and X. Xu, Exploration of intrinsic magnetic topological insulators in multiple-MnTe-intercalated topological insulator Bi_2Te_3 , *Applied Physics Letters* **124**, 223102 (2024).
- [42] M. Sahoo et al., Tuning strategy for Curie-temperature enhancement in the van der Waals magnet $\text{Mn}_{1+x}\text{Sb}_{2-x}\text{Te}_4$, *Materials Today Physics* **38**, 101265 (2023).
- [43] N. V. Selezneva, N. V. Baranov, E. M. Sherokalova, A. S. Volegov, and A. A. Sherstobitov, Multiple magnetic states and irreversibilities in the Fe_xTiS_2 system, *Phys. Rev. B* **104**, 064411 (2021).
- [44] J. Hu, T. J. Liu, B. Qian, and Z. Q. Mao, Coupling of electronic and magnetic properties in $\text{Fe}_{1+y}(\text{Te}_{1-x}\text{Se}_x)$, *Phys. Rev. B* **88**, 094505 (2013).
- [45] T. J. Liu et al., From $(\pi,0)$ magnetic order to superconductivity with (π,π) magnetic resonance in $\text{Fe}_{1.02}\text{Te}_{1-x}\text{Se}_x$, *Nature Mater* **9**, 718 (2010).
- [46] K. Binder and A. P. Young, Spin glasses: Experimental facts, theoretical concepts, and open questions, *Rev. Mod. Phys.* **58**, 801 (1986).
- [47] Sk. M. Yasin, V. Srinivas, S. Kasiviswanathan, M. Vagadia, and A. K. Nigam, Evidence for reentrant spin glass behavior in transition metal substituted Co-Ga alloys near critical concentration, *Journal of Magnetism and Magnetic Materials* **451**, 327 (2018).
- [48] C. A. Cardoso, F. M. Araujo-Moreira, V. P. S. Awana, E. Takayama-Muromachi, O. F. De Lima, H. Yamauchi, and M. Karppinen, Spin glass behavior in $\text{RuSrGd}_{1.5}\text{Ce}_{0.5}\text{Cu}_2\text{O}_{10-\delta}$, *Phys. Rev. B* **67**, 020407 (2003).
- [49] V. K. Anand, D. T. Adroja, and A. D. Hillier, Ferromagnetic cluster spin-glass behavior in PrRhSn_3 , *Phys. Rev. B* **85**, 014418 (2012).
- [50] T. Naka, T. Nakane, S. Ishii, M. Nakayama, A. Ohmura, F. Ishikawa, A. De Visser, H. Abe, and T. Uchikoshi, Cluster glass transition and relaxation in the random spinel CoGa_2O_4 , *Phys. Rev. B* **103**, 224408 (2021).
- [51] C. V. Topping and S. J. Blundell, A.C. susceptibility as a probe of low-frequency magnetic dynamics, *J. Phys.: Condens. Matter* **31**, 013001 (2019).
- [52] Y. Yeshurun, Spin-Glass-Ferromagnetic Critical Line in Amorphous Fe-Mn Alloys, *Phys. Rev. Lett.* **45**, 1366 (1980).

- [53] T. Gao, K. Nishimura, T. Namiki, and H. Okimoto, Reentrant spin-glass behavior induced by the frustration of Fe-Fe interactions in Laves phase $\text{Nb}_{1-x}\text{Hf}_x\text{Fe}_2$ alloys, *J. Appl. Phys.* **111**, 013913 (2012).
- [54] P. Cheng, W. Sun, Y. Fang, B. Kang, W. Lv, Q. Xiao, J. Zhang, and F. Chen, The evolution of spin-glass behavior in hexagonal $\text{Lu}_{1-x}\text{Ca}_x\text{MnO}_3$ single crystals, *Ceramics International* **46**, 15958 (2020).
- [55] R. Pradheesh, H. S. Nair, C. M. N. Kumar, J. Lamsal, R. Nirmala, P. N. Santhosh, W. B. Yelon, S. K. Malik, V. Sankaranarayanan, and K. Sethupathi, Observation of spin glass state in weakly ferromagnetic $\text{Sr}_2\text{FeCoO}_6$ double perovskite, *Journal of Applied Physics* **111**, 053905 (2012).
- [56] J. A. Mydosh, *Spin Glasses: An Experimental Introduction* (CRC Press, London, 2014).
- [57] J. L. Tholence, On the frequency dependence of the transition temperature in spin glasses, *Solid State Communications* **35**, 113 (1980).
- [58] J.-L. Tholence, Recent experiments about the spin-glass transition, *Physica B+C* **126**, 157 (1984).
- [59] G. Benka et al., Interplay of itinerant magnetism and spin-glass behaviour in $\text{Fe}_x\text{Cr}_{1-x}$, *Phys. Rev. Mater.* **6**, 044407 (2022).
- [60] M. A. V. Heringer, D. L. Mariano, D. C. Freitas, E. Baggio-Saitovitch, M. A. Continentino, and D. R. Sanchez, Spin-glass behaviour in $\text{Co}_3\text{Mn}_3(\text{O}_2\text{BO}_3)_2$ ludwigite with weak disorder, *Phys. Rev. Materials* **4**, 064412 (2020).
- [61] J. Liu, W. Xie, K. A. Gschneidner, G. J. Miller, and V. K. Pecharsky, Spin-glass behavior in a giant unit cell compound $\text{Tb}_{117}\text{Fe}_{52}\text{Ge}_{113.8(1)}$, *J. Phys.: Condens. Matter* **26**, 416003 (2014).
- [62] K. Górnicka, K. K. Kolincio, and T. Klimczuk, Spin-glass behavior in a binary Pr_3Ir intermetallic compound, *Intermetallics* **100**, 63 (2018).
- [63] F. Lüpke, M. Kolmer, J. Yan, H. Chang, P. Vilmercati, H. H. Weitering, W. Ko, and A.-P. Li, Anti-site defect-induced disorder in compensated topological magnet $\text{MnBi}_{2-x}\text{Sb}_x\text{Te}_4$, *Commun Mater* **4**, 82 (2023).
- [64] G. Shi, M. Zhang, D. Yan, H. Feng, M. Yang, Y. Shi, and Y. Li, Anomalous Hall Effect in Layered Ferrimagnet $\text{MnSb}_2\text{Te}_4^*$, *Chinese Phys. Lett.* **37**, 047301 (2020).
- [65] J. Li, Y. Li, S. Du, Z. Wang, B.-L. Gu, S.-C. Zhang, K. He, W. Duan, and Y. Xu, Intrinsic magnetic topological insulators in van der Waals layered MnBi_2Te_4 -family materials, *Science Advances* **5**, eaaw5685 (2019).
- [66] D. Zhang, M. Shi, T. Zhu, D. Xing, H. Zhang, and J. Wang, Topological Axion States in the Magnetic Insulator MnBi_2Te_4 with the Quantized Magnetoelectric Effect, *Phys. Rev. Lett.* **122**, 206401 (2019).

Figures:

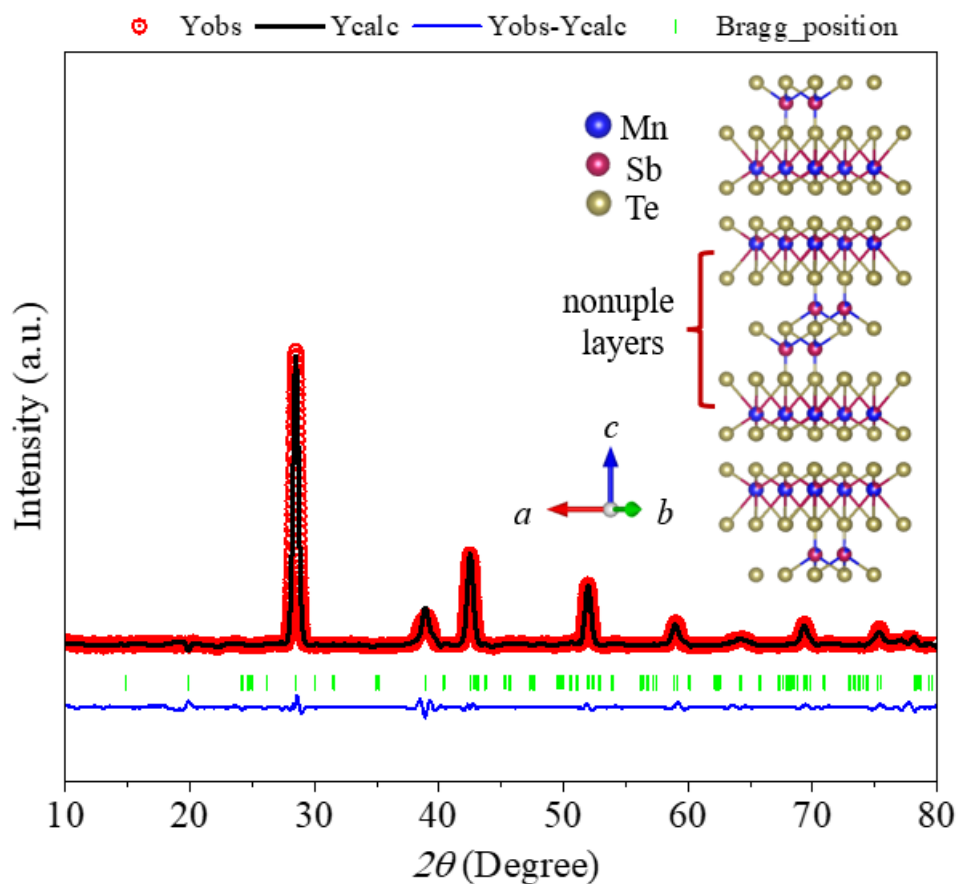


Fig. 1: Rietveld refined XRD pattern of $\text{Mn}_2\text{Sb}_2\text{Te}_5$ fitted with $P-3m1$ space group symmetry considering antisite disorder on Mn (2c) and Sb (2d) atomic sites, the inset is showing the corresponding unit cell showing partial occupancies on Mn (2c) and Sb (2d) atomic sites.

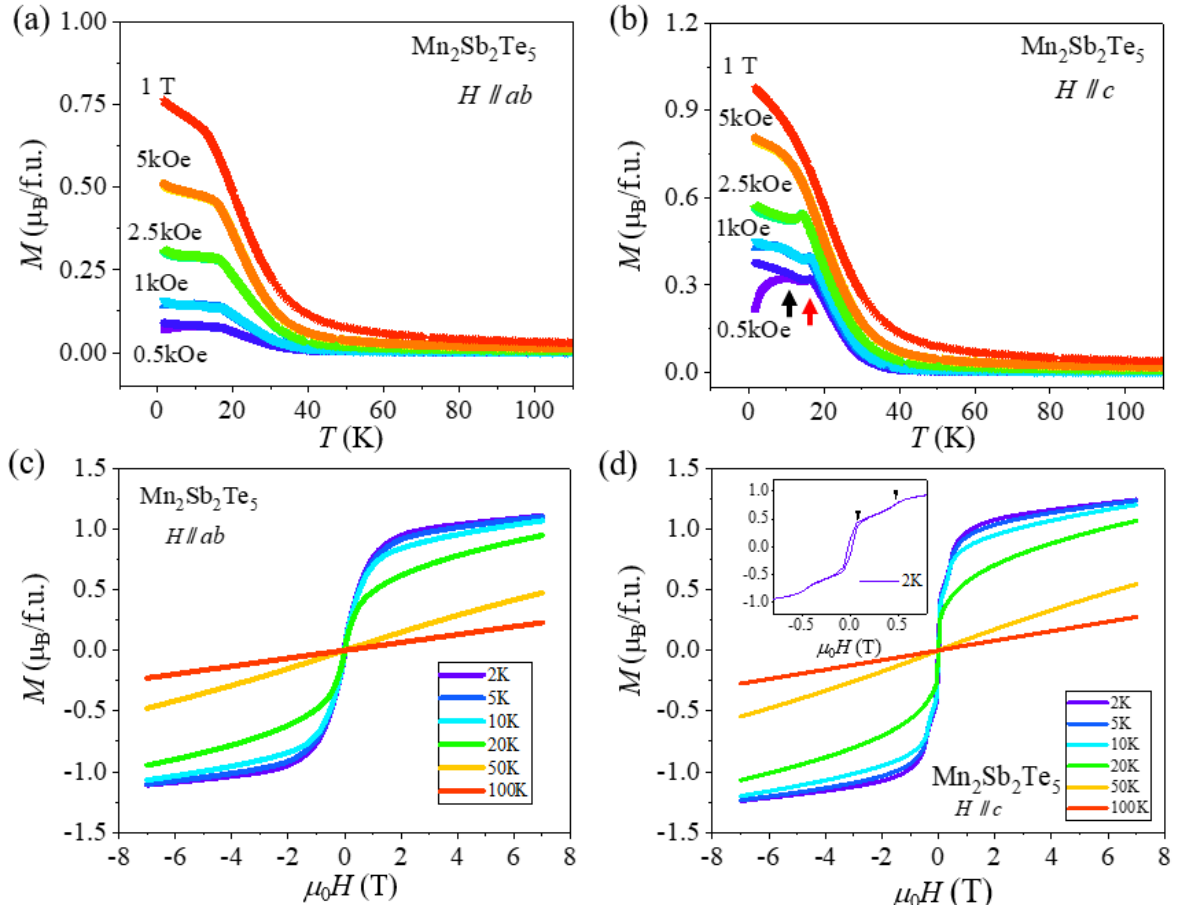


Fig. 2: DC magnetic moment (M) vs temperature (T) curve of $\text{Mn}_2\text{Sb}_2\text{Te}_5$ under various magnetic fields directed along (a) ab plane (b) c -axis. Isothermal magnetization vs applied magnetic field ($\mu_0 H$) curve of $\text{Mn}_2\text{Sb}_2\text{Te}_5$ at various temperatures with the applied magnetic field aligned along (c) ab plane (d) c axis.

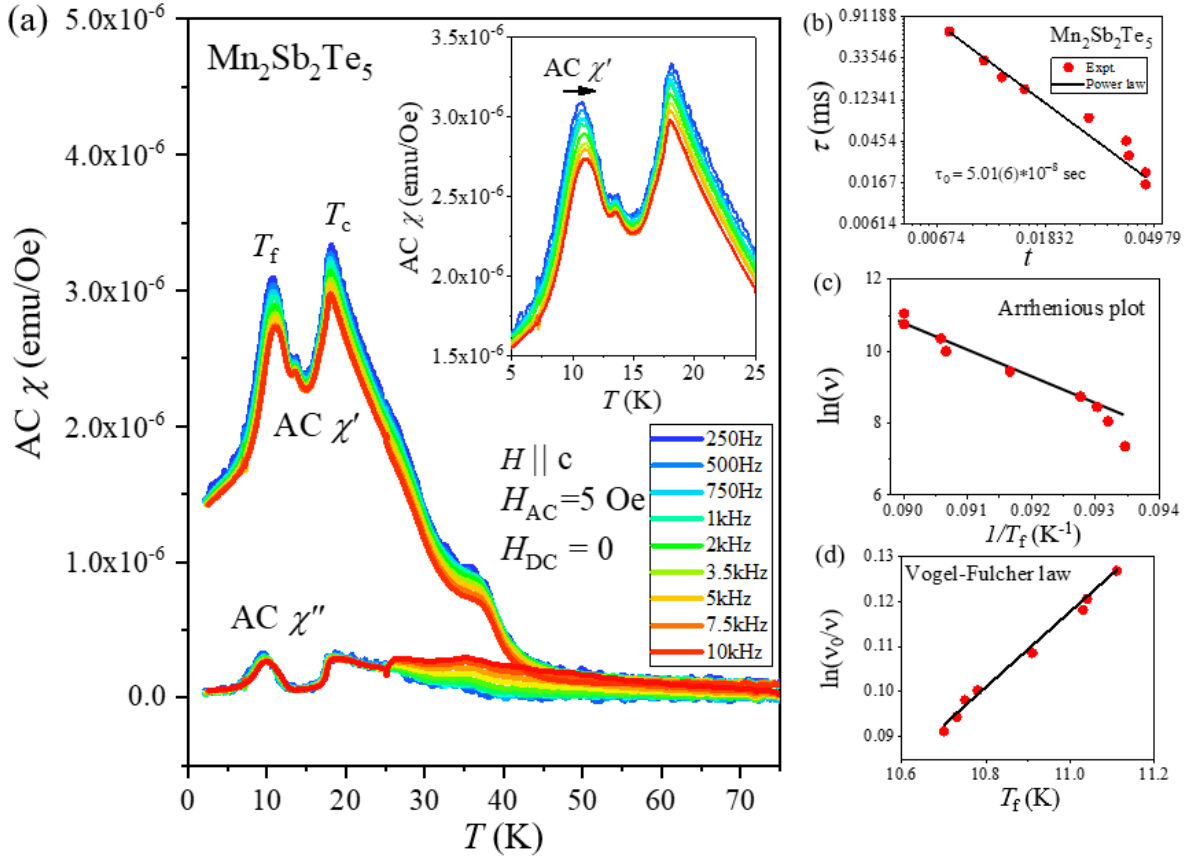


Fig. 3: (a) AC susceptibility vs T measurement of $\text{Mn}_2\text{Sb}_2\text{Te}_5$ single crystal performed under zero DC background an AC magnetic field of 5 Oe, while the frequency is changed from 250 Hz to 10 kHz. The inset shows the variation in real part of AC susceptibility ($\text{AC } \chi'$) with respect to temperature in the vicinity of spin glass transition at different AC frequencies. (b) The frequency dependence of freezing temperature (T_f) plotted as relaxation time (τ) vs reduced temperature (t). (c) The frequency dependence of T_f is plotted as $\ln(v)$ vs $1/T_f$, which is fitted with the Arrhenius law shown as black solid line. (d) The frequency dependence of T_f plotted as T_f vs $\ln(v_0/v)$, and fitted with Vogel-Fulcher law shown by black solid line.

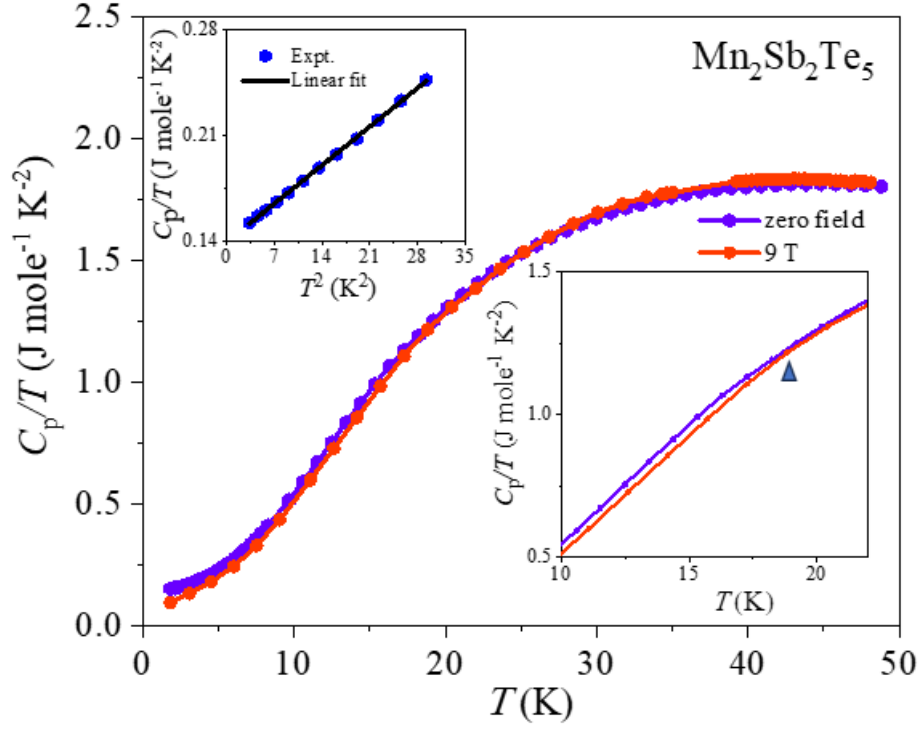


Fig. 4: Temperature dependence of specific heat plotted as C_p/T vs T , under the magnetic field of 0 T and 9 T. The upper left inset shows the C_p/T vs T^2 plot, fitted linearly as shown by the black solid line. The lower right inset shows the zoomed view of C_p/T vs T plot exhibiting the deviation of specific heat under zero magnetic field and a magnetic field of 9 T, evidencing the contribution of magnetism in specific heat of $\text{Mn}_2\text{Sb}_2\text{Te}_5$.

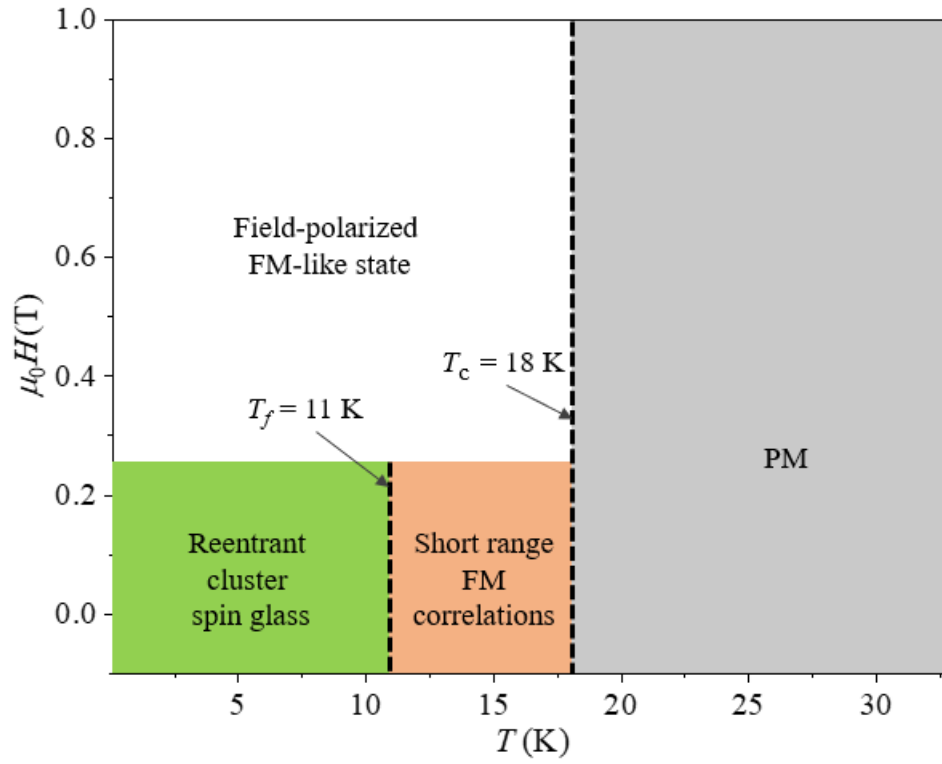


Fig. 5: H - T phase diagram describing different magnetic phases of $\text{Mn}_2\text{Sb}_2\text{Te}_5$.

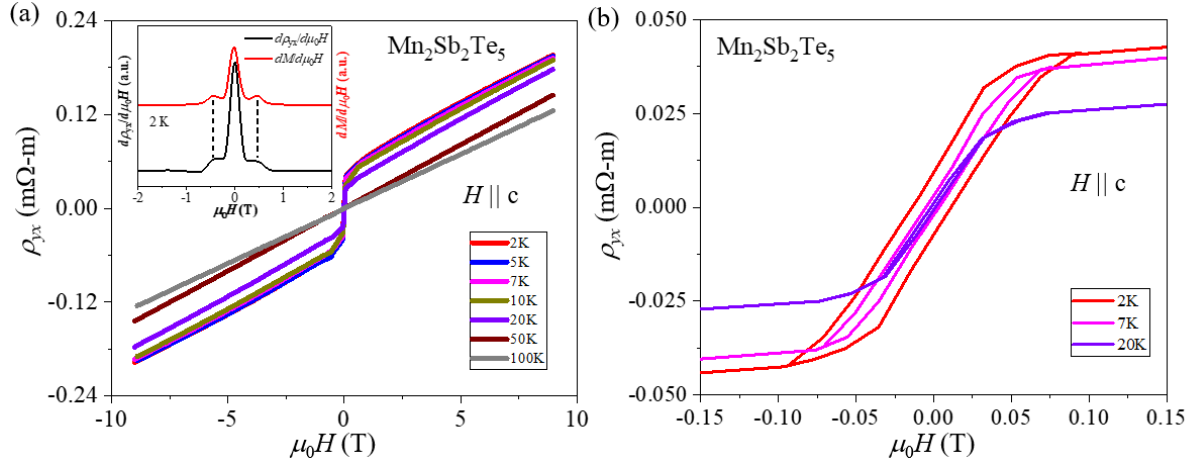


Fig. 6: (a) Hall resistivity (ρ_{yx}) as a function of applied magnetic field ($\mu_0 H$) at various temperatures, showing the presence of finite Hall resistivity in the absence of magnetic field evidencing the presence of the Anomalous Hall effect. The inset shows the first-order derivative of magnetization and Hall resistivity with respect to the applied magnetic field. (b) Zoomed view of ρ_{yx} vs $\mu_0 H$ plot in the vicinity of zero magnetic field showing the presence of hysteresis emerged due to intrinsic magnetization in $\text{Mn}_2\text{Sb}_2\text{Te}_5$.